ENGINEERING Information Technology & Electronic Engineering
https://www.academax.com/EITEE; https://www.engineering.org.cn
https://ieeexplore.ieee.org/xpl/RecentIssue.jsp?punumber=11344065
E-mail: eng.itee@zju.edu.cn

Engineering Journals
Available on IEEE Xplore®

Research Article
https://doi.org/10.1631/ENG.ITEE.2026.0129

Physics-based hierarchical identification and model-inversion feedforward control for CDC semi-active dampers

Shengdong YU[1,2,3], Chengdi ZHANG[3], Chao CHEN[1,2], Hongming ZHOU[3,4], Pengfei HAN[1,2]✉, Jinyu MA[4]✉

[1]*Zhejiang Yazhixing Automobile Components Co., Ltd., Wenzhou 325400, China*
[2]*Zhejiang Gold Intelligent Suspension Co., Ltd., Wenzhou 325200, China*
[3]*School of Mechanical and Electrical Engineering, Wenzhou University, Wenzhou 325035, China*
[4]*School of Intelligent Manufacturing, Wenzhou Polytechnic University, Wenzhou 325035, China*

Abstract: Semi-active suspension systems equipped with continuous damping control (CDC) dampers place stringent demands on accurate damper-level force tracking. However, the inherent hysteresis, compression–rebound asymmetry, and strong current dependence of the damper force make force control persistently challenging. This paper addresses this challenge with a four-component dynamic model that describes elastic restoring force, velocity-dependent viscous damping force, Bouc–Wen hysteresis force, and an additional force induced by directional asymmetry in a unified framework. Each current-dependent parameter is represented by an exponential saturation function, which naturally ensures bounded and monotonic coefficient mappings at the model level while avoiding empirical clipping. Because the four force components dominate in distinct operating regions, a three-stage hierarchical parameter identification method is further proposed to replace the coupled, single-step identification of all 20 parameters by direct global optimization. Based on the identified model, a feedforward inverse controller is constructed that combines online Bouc–Wen state reconstruction, passivity-based clipping, and Newton iteration to achieve real-time current solution and force tracking. Replacing equal-weight global fitting with the proposed saturation-mapped hierarchical scheme substantially reduces the identification error, from 0.155 to 0.079. In simulation, the inverse controller built on this model attains a force-tracking RMSE of 4.9 N, and hardware-in-the-loop experiments further verify the feasibility and effectiveness of the proposed framework under power-amplifier transport delay and other bench-level non-idealities.

Key words: CDC damper; Semi-active suspension; Hierarchical parameter identification; Bouc–Wen model; Model-inversion feedforward control; Force-sensor-free force tracking

1 Introduction

Semi-active suspension is generally regarded as a practical compromise between passive and fully active configurations, since it can adjust the damping force with low energy consumption and acceptable system complexity (Kimball et al., 2024). A recent review on advancements in semi-active automotive suspension systems with magnetorheological dampers reached a similar conclusion (Wang ZM et al., 2024), and a comparative study on a single-corner model also supported the engineering value of semi-active suspension control methods from a performance-evaluation perspective (Poussot-Vassal et al., 2012). In many production-oriented systems, the key controllable element is a continuous damping control (CDC) damper, for which physical modeling has been studied in the context of digital-twin applications driven by an electronically controlled proportional valve (Li T et al., 2023). As reviews on vibration-control strategies using magnetorheological-material actuators point out, the main difficulty lies not only in the upper-layer suspension controller but also in the damper-side force realization problem. Multi-stage hysteresis modeling of magnetorheological dampers has revealed that the output force depends on current, piston velocity, piston displacement, and loading history, rather than on a simple static current–force

✉ Pengfei HAN, han.pengfei@zj-gold.com.cn
✉ Jinyu MA, jinyuma@nuaa.edu.cn
Shengdong YU, https://orcid.org/0000-0003-2046-5676
Chengdi ZHANG, https://orcid.org/0009-0006-7800-3916
Chao CHEN, https://orcid.org/0009-0001-4506-0651
Pengfei HAN, https://orcid.org/0009-0007-5826-8340
Jinyu MA, https://orcid.org/0000-0003-3665-4797
CLC number: U463.33; TP273

Received: Apr. 30, 2026; Revision accepted: July 19, 2026;
Crosschecked: Sept. 10, 2026

© The Authors 2026. Published by Zhejiang University Press Co., Ltd. This is an open access article distributed under the terms of the CC BY-NC-ND license (https://creativecommons.org/licenses/by-nc-nd/4.0/)

relation (Li JH et al., 2023).

Under these conditions, an oversimplified damping model is insufficient for lower-layer control design. In the fundamentals of vehicle dynamics, linear or quasi-static models are often adopted first because of their analytical tractability (Gillespie, 1992). The method for random vibration of hysteretic systems proposed by Wen (1976), however, established that the force response can differ for the same instantaneous displacement and velocity if the loading path is different. The phenomenological model of a magnetorheological damper proposed by Spencer et al. (1997) became influential because it provided a compact description of this memory effect in controllable dampers. Muthalif et al. (2021) used particle swarm optimization to estimate parameters of magnetorheological damper models. Experimental validation of hybrid-damping-mode magnetorheological dampers has confirmed that semi-active dampers remain strongly nonlinear and current-sensitive over the full operating range (Lee and Oh, 2025). The key issue is therefore not whether hysteresis should be included, but how to represent it in a form suitable for both identification and control.

Parameter identification becomes particularly challenging when the elastic restoring force, viscous damping, hysteresis, and directional asymmetry are all retained in a single force model. Nondimensional analysis of semi-active electrorheological and magnetorheological dampers has also shown that controllable dampers are sensitive to parameter scaling and model structure (Wereley and Pang, 1998). At the suspension level, polytopic linear parameter-varying (LPV) approaches for intelligent automotive systems report a similar trade-off between modeling richness and calibration difficulty (Li PS et al., 2021). A review on LPV approaches for suspension systems likewise acknowledges that a richer model is usually harder to calibrate and to interpret physically (Sename, 2021). Recent semi-active suspension studies on inerter–spring–damper configurations continue to show strong parameter coupling when the damper-side physics are modeled in greater detail (Shen et al., 2024). This is why the design of a hierarchical controller, where different control layers address different physical mechanisms, remains attractive (Gáspár and Szabó, 2013). For CDC dampers, however, an identification method that explicitly exploits these separations while still yielding a model suitable for online inversion has not been fully developed.

The control literature points to a closely related limitation. Poussot-Vassal et al. (2008) made explicit that the dissipative constraint sits at the heart of any realizable force command. This is not a new observation: Karnopp (1995) had already formalized the rule that a semi-active device can only dissipate energy and cannot inject energy freely, while Fialho and Balas (2002) showed how the same constraint could be handled within a road-adaptive active-suspension design using LPV gain scheduling. The practical implication is clear: passivity enforcement is intrinsic to semi-active hardware and must be addressed at the controller level. Na et al. (2020) developed an approximation-free controller for full-car active suspension systems with unknown nonlinearities. On the sensing side, Qin et al. (2024) proposed a self-sensing approach for estimating suspension displacement and velocity in semi-active electromagnetic dampers. Specifically, for CDC hardware, Yuan et al. (2023) proposed a switched Takagi–Sugeno fuzzy controller with a current-input constraint, and Yuan et al. (2025) validated an asynchronous observer for CDC semi-active suspensions. The broader suspension-control community has also explored fractional-order control (Yin et al., 2024), multi-objective optimization (Cao et al., 2020), hierarchical preview control (Luan et al., 2025), hybrid ride-comfort and handling strategies (Wang F et al., 2025), and phase-deviation compensation with inertial suspension (Yang et al., 2024). What remains largely unaddressed, however, is a damper-level question of a different kind: how to construct a unified model that simultaneously guarantees bounded coefficient maps, identifiable parameters, and an online-invertible current–force relation subject to the passivity constraint.

This study addresses this gap by focusing on lower-layer current-to-force realization for a CDC damper, while leaving the upper-layer suspension law outside the scope. A four-component force model is assembled from an elastic restoring-force term, a velocity-dependent viscous damping term, a Bouc–Wen hysteretic term, and a compression–rebound asymmetric term. Every current-dependent coefficient is parameterized through an exponential saturation function, which keeps the resulting map bounded and monotonic by construction. Identification proceeds in three hierarchical stages, each targeting a region dominated by one or more force components to limit cross-coupling among parameters. The calibrated model then feeds a feedforward inverse controller that combines Newton-based current iteration, online Bouc–Wen state reconstruction, and passivity-based clipping. Bench experiments, ablation analysis, feedforward-control simulation, and hardware-in-the-loop (HIL) tests are reported to validate the approach.

2 Experimental setup and CDC damper characteristics

2.1 Experimental platform and test protocol

As shown in Fig. 1, the CDC damper is mounted on an MTS 850 servo-hydraulic rig (MTS Systems Corporation, USA). The rig applies sinusoidal displacement excitation under controlled laboratory conditions. Displacement, force, and current are sampled simultaneously at 10 kHz with 16-bit resolution so that the steep force variation near stroke reversal can be captured. A host PC sends the desired current command to a DC power amplifier through TCP/IP, and the amplifier drives the proportional solenoid valve in the damper.

Each test run follows a swept-sine protocol over the prescribed amplitude and frequency range. Each operating condition is recorded once, and temperature is not monitored. Repeatability and temperature effects are not evaluated. Piston displacement is measured by the built-in MTS linear variable differential Transformer (LVDT) encoder, velocity is obtained from the differentiated displacement signal after zero-phase low-pass filtering, damper force is recorded by the load cell, and the applied current is logged by the amplifier on the same time base. The test matrix combines several displacement amplitudes, excitation frequencies, and constant current levels to cover the main nonlinear characteristics of the CDC damper.

The 20 complete operating-condition segments are

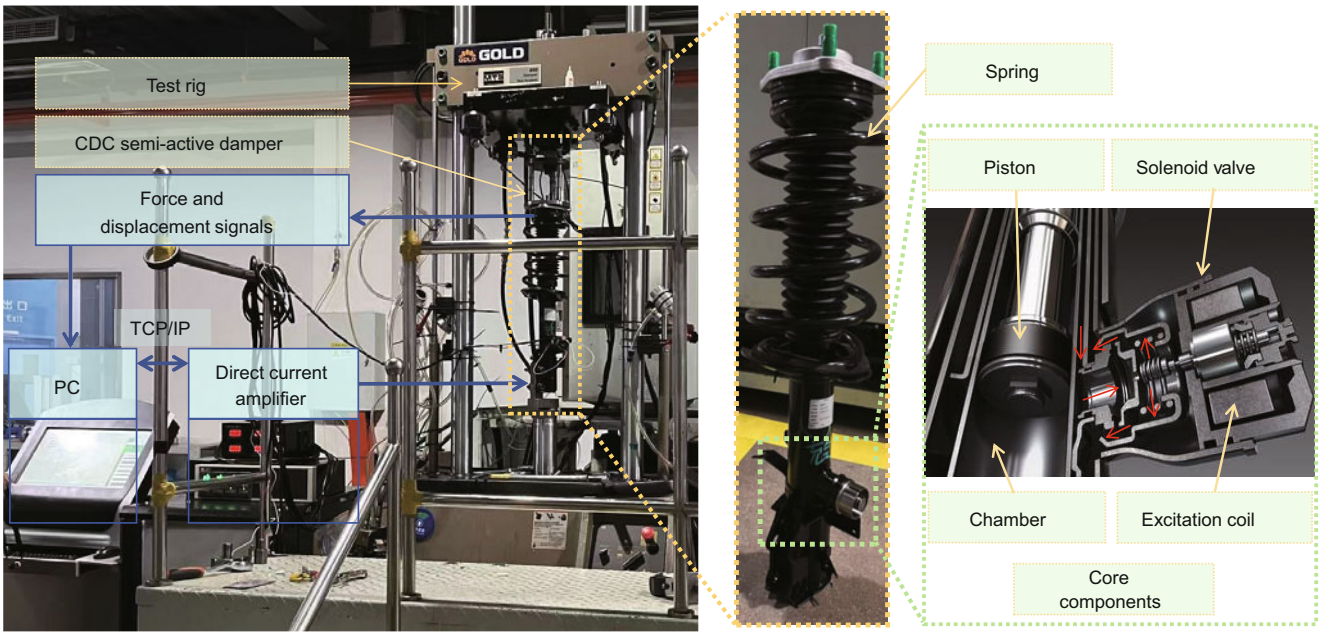


Fig. 1 Schematic of the continuous damping control (CDC) damper test platform

divided into 11 training segments and 9 held-out validation segments, with no individual segment split between the two sets. The load-cell force signal is used only for offline parameter fitting and performance evaluation and is not fed into the real-time control loop discussed in Section 5.

2.2 Observation of nonlinear characteristics and modeling implications

The bench data show five coupled nonlinear characteristics: displacement-related stiffness, velocity-dependent damping, current sensitivity, hysteresis, and compression–rebound asymmetry. These observations directly motivate the multi-component model in Section 3.

Fig. 2 shows that the force–displacement trajectory forms a closed loop with a non-zero area rather than a single-valued spring curve, which is evidence of energy dissipation over a cycle. The local slope also changes with the stroke position, so a simple linear spring is not sufficient. The restoring-force term must therefore reflect gas precharge, fluid compressibility, and seal friction and deformation.

Similar nonlinear behavior is observed in the force–velocity curves. As Fig. 3 shows, the force rises steeply at a low piston velocity and then rolls off at higher speeds, a saturation trend that a single linear viscous coefficient cannot reproduce. Increasing current shifts the whole force–velocity curve upward, but each additional current increment gives a smaller force increment, indicating valve-side saturation. This suggests that the current-dependent coefficients should be described by bounded, monotonic saturation maps rather than free polynomials.

One further observation links the two figures. Non-closure of the swept-sine trajectories alone does not establish hysteretic memory. Meanwhile, the rebound branch stays

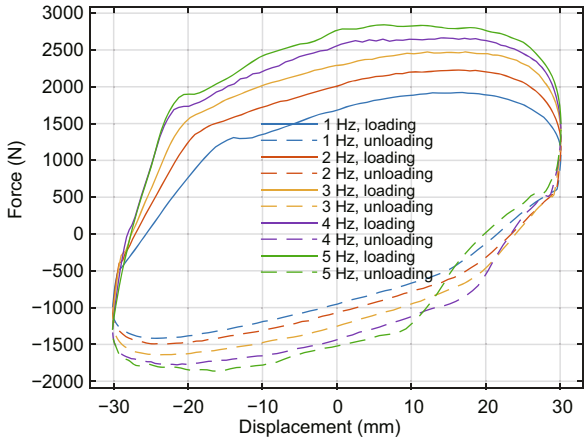


Fig. 2 Experimental force–displacement hysteresis loops under swept-sine excitation at 1 A

above the compression branch at matched absolute velocities, indicating a directional bias caused by asymmetric internal geometry. Any quasi-static symmetric damper model would miss both effects. For this reason, the total damper force is decomposed into four components: elastic restoring force, velocity-dependent viscous damping, Bouc–Wen hysteresis, and compression–rebound asymmetry.

3 Nonlinear dynamic model of the CDC damper

3.1 Overall modeling framework

For modeling, the damper–rig assembly is represented as a single-degree-of-freedom system:

$$m\ddot{x}(t) + F_{\mathrm{cdc}}(x(t), \dot{x}(t), z, I) = F_{\mathrm{in}}(t), \tag{1}$$

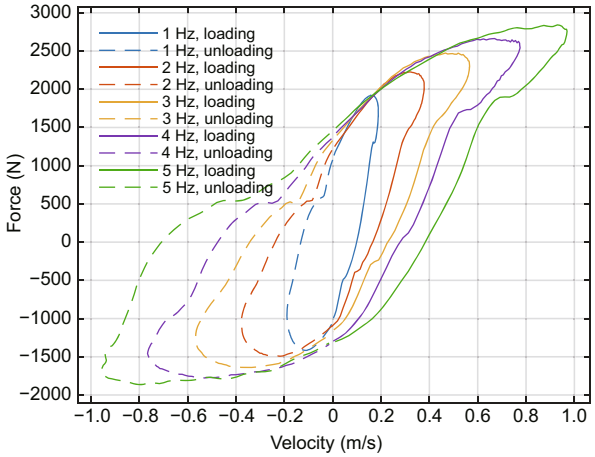


Fig. 3 Experimental force–velocity characteristics under swept-sine excitation at 1 A

where $m = 10$ kg is the equivalent mass, $x(t)$, $\dot{x}(t)$, and $\ddot{x}(t)$ denote the piston displacement, velocity, and acceleration, respectively, $F_{\mathrm{in}}(t)$ is the external excitation force, $F_{\mathrm{cdc}}(\cdot)$ is the CDC damper reaction force, z is the Bouc–Wen state variable, and I is the control current. In the following, for brevity, $x(t)$ and $\dot{x}(t)$ are written as x and $\dot{x}$, respectively.

For identification, the damper force is split into four parts:

$$F_{\mathrm{cdc}} = F_{\mathrm{s}}(x) + F_{\mathrm{d}}(\dot{x}, I) + F_{\mathrm{h}}(z, I) + F_{\mathrm{asym}}(\dot{x}, I). \tag{2}$$

The four terms are the elastic force $F_{\mathrm{s}}(x)$, damping force $F_{\mathrm{d}}(\dot{x}, I)$, Bouc–Wen force $F_{\mathrm{h}}(z, I)$, and asymmetric force $F_{\mathrm{asym}}(\dot{x}, I)$.

Substituting Eq. (2) into Eq. (1) gives

$$m\ddot{x}(t) + F_{\mathrm{s}}(x) + F_{\mathrm{d}}(\dot{x}, I) + F_{\mathrm{h}}(z, I) + F_{\mathrm{asym}}(\dot{x}, I) = F_{\mathrm{in}}(t). \tag{3}$$

This decomposition is retained because it separates the main mechanisms in a form directly usable by the staged procedure in Section 4.

3.2 Elastic restoring-force model

This term represents gas preload, fluid compressibility, and the low-speed restoring effect. A cubic expression is adopted:

$$F_{\mathrm{s}}(x) = a_0 + a_1 x_{\mathrm{mm}} + a_3 x_{\mathrm{mm}}^3. \tag{4}$$

Here, a_0 is the preload term, a_1 the linear stiffness, and a_3 the cubic correction. These parameters are independent of I. For numerical evaluation of the elastic polynomial, x_{mm} represents displacement in millimeters. The units of a_0, a_1, and a_3 are N, N/mm, and N/mm^3, respectively.

The cubic form is used here as a control-oriented approximation, not a universal elastic law. Within the tested range, it captures the main restoring-force nonlinearity with few interpretable parameters. At higher frequencies, stronger compressibility effects, or marked temperature variation, however, the restoring force may also depend on velocity, temperature-dependent stiffness, and seal friction. In such cases, $F_{\mathrm{s}}(x, \dot{x})$, piecewise polynomials, or temperature-dependent parameters may be required.

3.3 Damping-force model

The damping term represents the valve-related energy dissipation. A linear-quadratic expression is used:

$$F_{\mathrm{d}}(\dot{x}, I) = c_1(I)\dot{x} + c_2(I)|\dot{x}|\dot{x}. \tag{5}$$

The linear term $c_1(I)$ dominates at low speed, while the quadratic term $c_2(I)$ becomes more important as the piston speed increases.

Two current maps are compared. The baseline uses a polynomial:

$$c_1(I) = b_0 + b_1 I + b_2 I^2, \tag{6}$$

$$c_2(I) = d_0 + d_1 I + d_2 I^2. \tag{7}$$

These coefficient maps are empirical, but they do not limit the growth of the damping terms outside the fitted current range.

To overcome this limitation, an exponential saturation form is also considered:

$$c_1(I) = b_1 + b_2(1 - \mathrm{e}^{-b_3 I}), \tag{8}$$

$$c_2(I) = d_1 + d_2(1 - \mathrm{e}^{-d_3 I}). \tag{9}$$

The corresponding limits are $b_1 + b_2$ and $d_1 + d_2$, respectively. This form prevents unrealistic coefficient growth when the operating current goes beyond the main fitting range.

3.4 Bouc–Wen hysteretic-force model

The memory effect is described by a Bouc–Wen internal state. Similar Bouc–Wen-based hysteresis compensation and feedforward-control ideas have also been reported in piezo-driven precision mechanisms (Yu et al., 2021, 2022). These studies show that hysteresis modeling is not only a fitting issue, but also a control design issue when the model is later used for inversion or compensation. The hysteretic force is therefore written as a current-dependent gain multiplied by the internal variable z:

$$F_{\mathrm{h}}(z, I) = k_{\mathrm{h}}(I) z, \tag{10}$$

where $k_{\mathrm{h}}(I)$ is the hysteretic gain. The evolution of z is given by

$$\dot{z} = A\dot{x} - \beta|\dot{x}||z|^{n-1}z - \gamma\dot{x}|z|^n, \tag{11}$$

where A controls the initial slope, β and γ govern the loop shape, and n controls the transition sharpness.

Again, two current maps are tested. The quadratic form is

$$k_{\mathrm{h}}(I) = h_0 + h_1 I + h_2 I^2, \tag{12}$$

and the saturation form is

$$k_{\mathrm{h}}(I) = h_1 + h_2(1 - \mathrm{e}^{-h_3 I}). \tag{13}$$

The saturation coefficients keep the hysteretic gain bounded as the current increases.

3.5 Asymmetric additional-force model

Directional asymmetry is represented through a smooth hyperbolic-tangent correction:

$$F_{\mathrm{asym}}(\dot{x}, I) = r(I)\tanh\left(\frac{\dot{x}}{v_{\mathrm{s}}}\right), \tag{14}$$

where $r(I)$ controls the bias magnitude and v_{s} controls the transition near zero speed. The polynomial form is

$$r(I) = r_0 + r_1 I + r_2 I^2, \tag{15}$$

and the saturation form is

$$r(I) = r_1 + r_2(1 - \mathrm{e}^{-r_3 I}). \tag{16}$$

3.6 Model summary

Eqs. (3) and (11) together define the proposed damper model. Under saturation parameterization, the full model contains 20 parameters: 3 for the elastic term, 6 for the damping term, 7 for the hysteretic term, and 4 for the asymmetric term. Section 4 identifies these parameters in three physically motivated stages.

4 Hierarchical parameter-identification strategy based on physical mechanisms

4.1 Analysis of the identification problem

Directly estimating 20 coupled parameters in one optimization step is numerically difficult. The search space is large, local minima are common, and the physical meaning of each force term becomes unclear during the fitting process.

A mechanism-based split provides a more reliable solution. Near zero velocity, the elastic part is dominant. After this part is removed, the damping term becomes much easier to identify. After both components are separated, the remaining residual is governed mainly by hysteresis and directional asymmetry. The proposed identification strategy therefore follows this physical order.

4.2 Three-stage implementation of the saturation-mapped hierarchical identification method

The full saturation-mapped model is identified in three stages.

Stage 1 estimates the elastic parameters (a_0, a_1, a_3). Samples in the near-zero-velocity region are selected first. In this region, the velocity-related terms are small, so the measured force is dominated by the elastic restoring term:

$$F_{\mathrm{cdc}} \approx F_{\mathrm{s}}(x) = a_0 + a_1 x_{\mathrm{mm}} + a_3 x_{\mathrm{mm}}^3. \tag{17}$$

The selected samples have velocity magnitudes below the 25^{th} percentile. This threshold is treated as an engineering initial choice for stage 1, not a universally optimal constant. It retains enough samples for stable estimation while reducing contamination from damping, hysteresis, and asymmetry. Additional checks show that changing this percentile modifies the stage-1 sample set but does not produce a clear monotonic change in the final three-stage error. Therefore, the 25^{th} percentile is used here as a practical compromise; for other datasets or dampers, it should be reselected by threshold scanning or cross-validation. An initial estimate is obtained using least squares, and the parameter values are then refined using a hybrid particle swarm optimization–simplex method.

Stage 2 estimates the damping parameters $(b_1, b_2, b_3, d_1, d_2, d_3)$. The fitted elastic force is first removed from the raw measurement so that the residual is governed mainly by the damping term:

$$F_{\mathrm{res,d}}(t) = F_{\mathrm{meas}}(t) - F_{\mathrm{s}}(x). \tag{18}$$

The saturation damping model is fitted to that residual:

$$\begin{aligned} F_{\mathrm{d}}(\dot{x}, I) = {} & [b_1 + b_2(1 - \mathrm{e}^{-b_3 I})]\dot{x} \\ & + [d_1 + d_2(1 - \mathrm{e}^{-d_3 I})]|\dot{x}|\dot{x}. \end{aligned} \tag{19}$$

The same hybrid optimizer is used to identify these six damping parameters. Although $F_{\mathrm{res,d}}$ is damping-dominated, it is not guaranteed to be free of hysteretic or asymmetric remnants. Accordingly, the stage-2 results are interpreted as an equivalent damping representation under residual coupling, while the remaining path-dependent and directional effects are absorbed in stage 3.

Stage 3 estimates the remaining 11 parameters related to hysteresis and asymmetry. At this point, both the elastic and damping parts are removed first, leading to the residual:

$$F_{\mathrm{res,h}}(t) = F_{\mathrm{meas}}(t) - F_{\mathrm{s}}(x) - F_{\mathrm{d}}(\dot{x}, I). \tag{20}$$

The remaining model terms are then fitted to this residual:

$$F_{\mathrm{res,h}} \approx k_{\mathrm{h}}(I) z + r(I)\tanh(\dot{x}/v_{\mathrm{s}}). \tag{21}$$

At this stage, Eq. (11) must be integrated for every trial parameter set. Particle swarm optimization is used for the global search, and simplex is used for local refinement. Related nonlinear identification and robust tracking problems in precision actuation have also shown that richer hysteretic models may improve tracking quality, but usually at the cost of a higher computational burden (Ma et al., 2023; Yu et al., 2024).

Remark 1 This stage is the most computationally expensive because the hysteretic state must be integrated repeatedly during optimization.

The computational burden of stage 3 is purely offline. Once the parameters are identified, the online controller no longer runs particle swarm optimization or simplex; it only updates the Bouc–Wen state and solves a scalar inverse problem for each sample. Hence, the large calibration cost does not directly transfer to real-time control.

4.3 Design of comparison algorithms: a systematic ablation study

Three comparison models are introduced for ablation analysis. The polynomial hierarchical model maintains the three-stage structure and the asymmetric term but replaces the saturation maps with quadratic polynomials. The basic hierarchical model uses staged identification and quadratic polynomial current maps without the asymmetric term. The globally synchronous model uses the same force components and current maps as the basic hierarchical model, but identifies its parameters jointly.

These models support pairwise comparisons of the identification strategy, asymmetry, and current-map form. In this way, the roles of staged decomposition, directional asymmetry, and saturation mapping can be examined separately. The quantitative comparison is given in Section 6.

5 Feedforward controller design based on model inversion

5.1 Definition of the control problem and signal-chain architecture

A semi-active suspension typically contains two control layers. The upper layer computes the desired damping force $F_{\mathrm{des}}(t)$ from vehicle-state measurements and the chosen suspension-control law, while the lower layer determines the current $I(t)$ required for the CDC damper to realize that force accurately.

The lower-layer task is handled by inverting the identified damper model. The controller takes $F_{\mathrm{des}}(t)$ together with the measured displacement $x(t)$ and velocity $\dot{x}(t)$ as inputs, and outputs the current command $I(t)$. Since no force sensor is available online, the performance of the inverse controller depends directly on model accuracy. Inverse-model-assisted feedforward control and robust motion compensation have also been studied in other nonlinear actuator systems (Yu et al., 2022, 2024; Ma et al., 2023). From an implementation point of view, the key issue is not only fitting accuracy, but also whether the current–force relationship remains regular over the admissible operating range.

Several internal signals define this calculation chain. The starting point is the desired damping force $F_{\mathrm{des}}(t)$ generated by the upper-level controller. The passivity condition is then checked. If $F_{\mathrm{des}}\dot{x} \le 0$, the requested force is dissipative and can be kept directly, so the realizable force request satisfies $F_{\mathrm{cmd}}(t) = F_{\mathrm{des}}(t)$. If $F_{\mathrm{des}}\dot{x} > 0$, the request would inject energy into the suspension. Since a semi-active device cannot provide active energy input, the controller applies $I_{\min}$ and bypasses inversion for that sampling instant.

If passivity is satisfied, the algorithm subtracts the elastic component and obtains $F_{\mathrm{target}}(t)$, namely the exact force that must be generated by the current-dependent terms of the model, with $F_{\mathrm{target}} = F_{\mathrm{cmd}} - F_{\mathrm{s}}(x)$. The feedforward current $I_{\mathrm{ff}}(t)$ is then obtained by solving $\Phi(I_{\mathrm{ff}}) = F_{\mathrm{target}}$. This raw solution is finally clipped to satisfy the hardware limits, yielding $I(t) = \mathrm{sat}(I_{\mathrm{ff}}, I_{\min}, I_{\max})$. A separate variable, $F_{\mathrm{actual}}(t)$, denotes the physical damper force used only for offline evaluation and never enters the real-time control loop.

The resulting signal chain can therefore be summarized as $F_{\mathrm{des}} \to F_{\mathrm{cmd}} \to F_{\mathrm{target}} \to I_{\mathrm{ff}} \to I(t) \to F_{\mathrm{actual}}$. In this way, an unconstrained theoretical force request is transformed into a physically admissible and numerically solvable hardware command.

5.2 Model inversion and the current response function

Starting from the four-component damper-force model in Eq. (2), let $F_{\mathrm{actual}} = F_{\mathrm{cmd}}$ and move the elastic term $F_{\mathrm{s}}(x)$, which does not depend on current, to the right-hand side:

$$F_{\mathrm{actual}} = F_{\mathrm{s}}(x) + F_{\mathrm{d}}(\dot{x}, I) + F_{\mathrm{h}}(z, I) + F_{\mathrm{asym}}(\dot{x}, I). \tag{22}$$

The corresponding target force, namely the force to be generated by the current-dependent part of the model, is then written as

$$\begin{aligned} F_{\mathrm{target}}(t) &= F_{\mathrm{cmd}}(t) - F_{\mathrm{s}}(x) \\ &= F_{\mathrm{cmd}}(t) - (a_0 + a_1 x_{\mathrm{mm}} + a_3 x_{\mathrm{mm}}^3). \end{aligned} \tag{23}$$

Only the elastic term is moved to the right-hand side. The damping, hysteretic, and asymmetric contributions all remain in the current-dependent part, which is grouped into the current response function $\Phi(I)$:

$$\Phi(I) = c_1(I)\dot{x} + c_2(I)|\dot{x}|\dot{x} + k_{\mathrm{h}}(I)z + r(I)\tanh\left(\frac{\dot{x}}{v_{\mathrm{s}}}\right). \tag{24}$$

$\Phi(I)$ denotes the nonlinear current-to-force relationship, which must be inverted at each control instant. The current response can be decomposed into four components:

$$\Phi(I) = \Phi_{\mathrm{d1}}(I) + \Phi_{\mathrm{d2}}(I) + \Phi_{\mathrm{h}}(I) + \Phi_{\mathrm{a}}(I), \tag{25a}$$

where the individual components are defined as follows:

$$\Phi_{\mathrm{d1}}(I) = \left[b_1 + b_2\left(1 - \mathrm{e}^{-b_3 I}\right)\right]\dot{x}, \tag{25b}$$

$$\Phi_{\mathrm{d2}}(I) = \left[d_1 + d_2\left(1 - \mathrm{e}^{-d_3 I}\right)\right]|\dot{x}|\dot{x}, \tag{25c}$$

$$\Phi_{\mathrm{h}}(I) = \left[h_1 + h_2\left(1 - \mathrm{e}^{-h_3 I}\right)\right] z, \tag{25d}$$

$$\Phi_{\mathrm{a}}(I) = \left[r_1 + r_2\left(1 - \mathrm{e}^{-r_3 I}\right)\right]\tanh\left(\frac{\dot{x}}{v_{\mathrm{s}}}\right). \tag{25e}$$

The feedforward computation is therefore reduced to a scalar nonlinear equation:

$$\Phi(I_{\mathrm{ff}}) = F_{\mathrm{target}}(t), \tag{26}$$

where I_{ff} denotes the feedforward current to be applied by the controller. The reliability of the whole lower-layer control strategy depends on solving this equation stably.

1. Derivative of the current response. Differentiating Φ with respect to I gives

$$\begin{aligned} \frac{\mathrm{d}\Phi}{\mathrm{d}I} &= b_2 b_3 \mathrm{e}^{-b_3 I}\dot{x} + d_2 d_3 \mathrm{e}^{-d_3 I}|\dot{x}|\dot{x} \\ &\quad + h_2 h_3 \mathrm{e}^{-h_3 I} z + r_2 r_3 \mathrm{e}^{-r_3 I}\tanh(\dot{x}/v_{\mathrm{s}}). \end{aligned} \tag{27}$$

Because z may change sign, positive coefficient pairs alone do not establish a fixed sign for $\Phi'(I)$; global monotonicity and uniqueness are therefore not claimed.

2. Newton iteration. The inversion equation is solved by Newton's method:

$$I_{k+1} = I_k - \frac{\Phi(I_k) - F_{\mathrm{target}}}{\Phi'(I_k)}, \tag{28}$$

where I_k is the iteration at step k, and $\Phi'(I_k)$ is the derivative in Eq. (27) evaluated at that point. The iteration is initialized by the current value from the previous sampling instant, $I_0 = I(t - \Delta t)$, which improves convergence through temporal continuity. The stopping criterion is $|\Phi(I_k) - F_{\mathrm{target}}| < \epsilon_{\mathrm{tol}}$, with a maximum of $N_{\max}$ iterations. In practice, $\epsilon_{\mathrm{tol}} = 1$ N

and $N_{\max} = 10$ balance accuracy and real-time burden. A 1-N residual is already small for the CDC-damper force range, and a much smaller tolerance would bring limited benefit once the model error, sensor noise, and driver dynamics are considered. By local linearization, the residual tolerance corresponds approximately to a current error $\delta I \approx \epsilon_{\text{tol}}/|\Phi'(I)|$, which should remain below the effective current resolution of the driver. The cap $N_{\max} = 10$ is conservative, whereas the actual iteration count is usually only two to four, compatible with a 1-ms control period. Thus, the online load is dominated by $O(N_{\text{Newton}})$ scalar function evaluations plus one Bouc–Wen state update per sample.

Fig. 4 illustrates the overall feedforward architecture. After passivity checking, the elastic compensation block subtracts $F_{\text{s}}(x)$ from F_{cmd} to form F_{target}. The measured signals x and $\dot{x}$ enter both the elastic compensation block and the current response function $\Phi(I)$, while the Bouc–Wen observer supplies the online estimate of z. Only the main signal paths are shown; the complete relations are given in Eqs. (29)–(31) and Section 5.4.

5.3 Handling of engineering constraints

Before the controller is implemented on hardware, three engineering issues must be addressed:

1. Bouc–Wen state reconstruction. The internal state $z(t)$ is not directly measurable. It is updated online using a forward-Euler discretization of the Bouc–Wen ordinary differential equation:

$$z(t_k) = z(t_{k-1}) + \Delta t\, \Delta z(t_{k-1}), \tag{29a}$$

where the individual components are defined as follows:

$$\Delta z(t_{k-1}) = \Delta z_A(t_{k-1}) + \Delta z_\beta(t_{k-1}) + \Delta z_\gamma(t_{k-1}), \tag{29b}$$

$$\Delta z_A(t_{k-1}) = A\dot{x}(t_{k-1}), \tag{29c}$$

$$\Delta z_\beta(t_{k-1}) = -\beta|\dot{x}(t_{k-1})||z(t_{k-1})|^{n-1} z(t_{k-1}), \tag{29d}$$

$$\Delta z_\gamma(t_{k-1}) = -\gamma\dot{x}(t_{k-1})|z(t_{k-1})|^{n}. \tag{29e}$$

This update law has low computational cost and provides enough accuracy for inversion under the 1-ms sampling period used in this study.

2. Current saturation. The physical valve operates within a finite current range, and the command is therefore saturated as follows:

$$I(t) = \text{sat}(I_{\text{ff}}(t), I_{\min}, I_{\max}), \tag{30}$$

with $I_{\min} = 0$ A and $I_{\max} = 2$ A.

3. Passivity enforcement. A semi-active damper can dissipate energy, but it cannot inject energy into the suspension. Whenever the desired force and the velocity have the same sign, the upper controller is effectively asking for active power input. In this case, the current is set to $I_{\min}$ and the inversion stage is bypassed:

$$I(t) = \begin{cases} I_{\min}, & \text{if } F_{\text{des}}(t)\dot{x}(t) > 0, \\ \text{sat}(I_{\text{ff}}, I_{\min}, I_{\max}), & \text{otherwise.} \end{cases} \tag{31}$$

Remark 2 This constraint reflects the essential distinction between a CDC damper and a fully active actuator. It limits the set of achievable force commands but must be enforced for semi-active hardware.

5.4 Algorithmic procedure

The control routine is executed at each sampling instant t_k. The first step updates the hysteretic state $z(t_k)$ from $z(t_{k-1})$ using Eqs. (29a)–(29e). The passivity condition is then checked. If $F_{\text{des}}(t_k)\dot{x}(t_k) > 0$, the requested force would inject energy into the system. Since the CDC damper cannot generate active power, the controller sets $I(t_k) = I_{\min}$ for that step; otherwise, the desired force is passed to $F_{\text{cmd}}(t_k)$ directly, i.e., Eq. (31).

Next, the elastic component is removed from the command force. Using Eq. (23), the controller computes F_{target} by subtracting $a_0 + a_1 x_{\text{mm}}(t_k) + a_3 x_{\text{mm}}^3(t_k)$. The remaining force is the part that must be produced by the damping, hysteretic, and asymmetric terms.

The current is then obtained by the Newton iteration. The solver uses Eqs. (25a)–(25e) with the updated state $z(t_k)$. The initial guess is taken as the previous current, $I(t_{k-1})$. The iteration stops when $|\Phi(I) - F_{\text{target}}| < \epsilon_{\text{tol}}$, where ϵ_{tol} follows the trade-off between accuracy and computational burden as discussed in Section 5.2. Similar iterative or robust tracking procedures have been reported for piezoactuated precision systems (Yu et al., 2021; Ma et al., 2023). In this sense, the inverse solver is not just a numerical step. It is part of the actuator-side control design and directly benefits from a model with bounded coefficients and clearly separated physical roles.

The final output is clipped to the hardware range. Eq. (30) limits $I(t_k)$ between $I_{\min}$ and $I_{\max}$ before the command is sent to the amplifier.

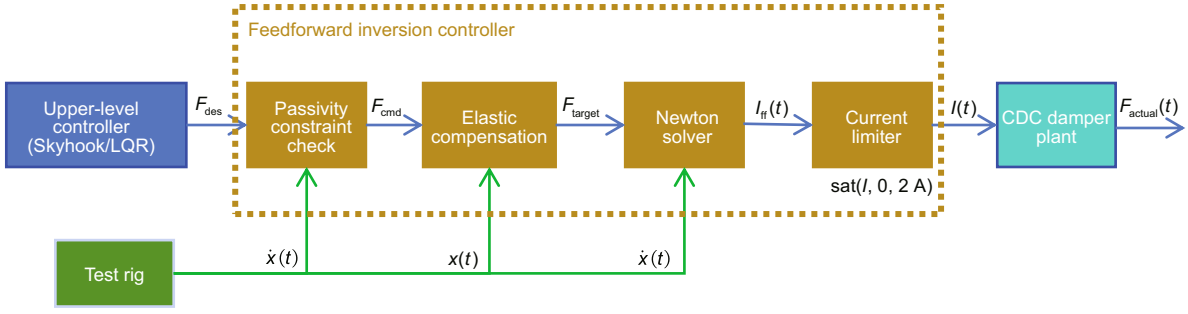


Fig. 4 Block diagram of the feedforward control system

6 Results and discussion

6.1 Parameter identification results

The four identification strategies are tested on the same dataset. Table 1 lists the parameter values.

For the saturation-mapped hierarchical model, the damping saturation rates remain positive, with $b_3 = 0.1848$ and $d_3 = 19.33$, which is consistent with a monotonic current-dependent increase in effective damping that gradually approaches a finite limit. The hysteretic gain also shows a positive saturation rate, $h_3 = 0.6216$. In addition, the asymmetric offset $r_1 = 377.43$ N at zero current indicates that the rebound–compression bias already exists in the hardware before the control current increases.

6.2 Model accuracy and ablation analysis

Table 2 summarizes the identification errors for the four model structures. The saturation-mapped hierarchical model performs best, with TrainWeighted, ValidationWeighted, and AllEqual decreasing to 0.049, 0.116, and 0.079, respectively. Relative to the globally synchronous model, whose corresponding metrics are 0.108, 0.218, and 0.155, these values represent reductions of 55%, 47%, and 49%, respectively.

The proposed model has a training–validation gap of 0.067, versus 0.110 for the globally synchronous model, 0.126 for the polynomial hierarchical model, and 0.522 for the basic hierarchical model. The saturation-mapped formulation thus achieves the smallest gap, indicating better performance on the held-out validation subset.

The validation weighted objective is 0.672 for the basic hierarchical model and 0.218 for the globally synchronous model; staged identification alone does not improve this metric in the tested comparison.

When the asymmetric term is restored together with polynomial current maps, ValidationWeighted decreases to 0.308. Replacing the polynomial maps with saturation maps reduces it further to 0.116. This comparison shows that bounded current-dependent parameterizations describe the valve behavior better than unbounded polynomial maps.

The validation results may be associated with bounded current maps and the asymmetric term. Exponential saturation keeps each current-dependent coefficient bounded and monotonic, suppressing nonphysical extrapolation. Retaining the compression–rebound asymmetric term prevents the directional bias from being absorbed by the damping or hysteretic terms. Together, these features explain the lower validation error and smaller training–validation gap.

The figures are consistent with the tabulation results. In Figs. 5 and 6, the saturation-mapped model follows the loop envelope, branch separation, and reversal region more closely than the other models. Figs. 7 and 8 show the same results

Table 1 Model parameters identified by the four strategies

Parameter category	Parameter	Globally synchronous	Basic hierarchical	Polynomial hierarchical	Saturation-mapped hierarchical
Elastic term	a_0 (N)	119.79	−20.95	26.12	37.79
	a_1 (N/mm)	23.66	27.48	31.98	28.81
	a_3 (N/mm^3)	0.0115	−0.0053	−0.0067	−0.0029
Damping term	Polynomial b_0 / Saturation b_1	2357.2	2497.0	4175.8	0.0145
	Polynomial b_1 / Saturation b_2	0	0	858.68	7938.0
	Polynomial b_2 / Saturation b_3	604.07	1933.8	16.85	0.1848
	Polynomial d_0 / Saturation d_1	4.28	0.199	54.03	3.24×10^{-6}
	Polynomial d_1 / Saturation d_2	0	0	4.20	3.82×10^{-5}
	Polynomial d_2 / Saturation d_3	100	0	17.07	19.33
Hysteretic term	Polynomial h_0 / Saturation h_1	7.54×10^7	6.60×10^7	2.82×10^7	6948.5
	Polynomial h_1 / Saturation h_2	1151.6	3.41×10^5	8.92×10^7	6.70×10^7
	Polynomial h_2 / Saturation h_3	1.00×10^8	3.23×10^7	1.37	0.6216
	A	4.42×10^{-4}	1.00×10^{-4}	1.00×10^{-4}	3.33×10^{-4}
	β	8000	1.00×10^{-4}	3612.6	247.69
	γ	1.00×10^{-4}	8000	1653.0	2085.3
	n	1.27	3.00	2.23	1.44
Asymmetric term	Polynomial r_0 / Saturation r_1	0	0	−4630.2	377.43
	Polynomial r_1 / Saturation r_2	0	0	4787.2	1778.3
	Polynomial r_2 / Saturation r_3	0	0	0.897	0.3672
	v_s	1	1	2.59	0.1267

For "Polynomial x / Saturation y" in the damping, hysteretic, and asymmetric categories, x corresponds to the quadratic polynomial parameters in columns 3–5 and y to the exponential saturation parameters in the last column

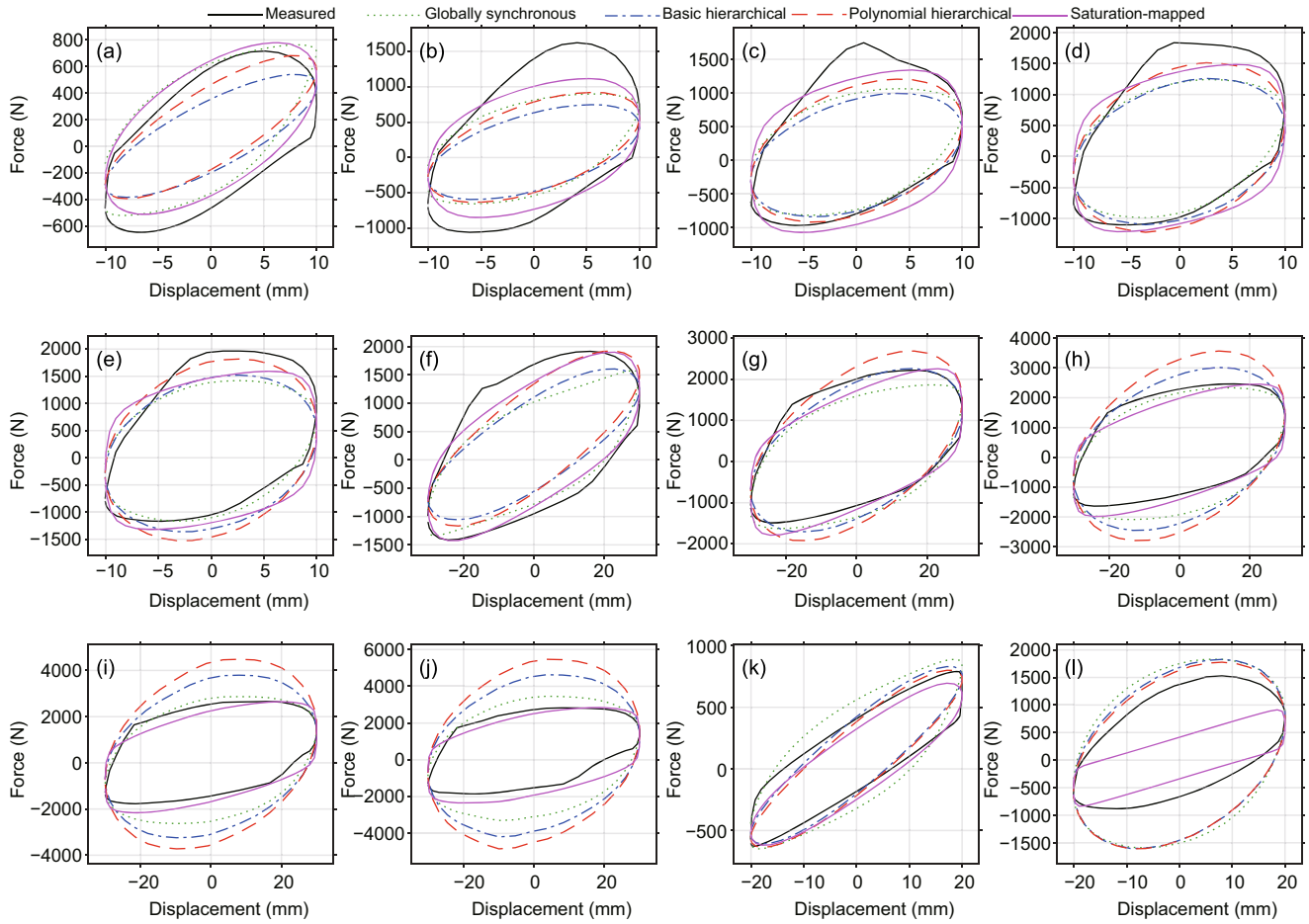


Fig. 5 Force–displacement loops for the four models and measurement data: (a) $I = 1$ A, 1 Hz; (b) $I = 1$ A, 2 Hz; (c) $I = 1$ A, 3 Hz; (d) $I = 1$ A, 4 Hz; (e) $I = 1$ A, 5 Hz; (f) $I = 0.5$ A, 1 Hz; (g) $I = 0.5$ A, 2 Hz; (h) $I = 0.5$ A, 3 Hz; (i) $I = 0.5$ A, 4 Hz; (j) $I = 0.5$ A, 5 Hz; (k) $I = 0$ A, 1 Hz; (l) $I = 0$ A, 5 Hz

Table 2 Comparison of generalization metrics for the four identification models

Model	TrainWeighted	ValidationWeighted	AllEqual
Globally synchronous	0.108	0.218	0.155
Basic hierarchical	0.150	0.672	0.367
Polynomial hierarchical	0.182	0.308	0.234
Saturation-mapped hierarchical	**0.049**	**0.116**	**0.079**

TrainWeighted and ValidationWeighted evaluate the same composite objective on the 11 training segments and 9 held-out operating-condition segments using condition weights. AllEqual evaluates it over all 20 segments with equal segment weights. The identified parameters are fixed; lower values indicate better agreement. The best results are in bold

in terms of RMSE, namely a lower mean error together with a tighter spread across operating conditions.

6.3 Robustness analysis under multi-objective optimization

Table 3 examines the robustness of the saturation-mapped hierarchical model with respect to the multi-objective weighting choice. The loop objective remains at 0.0334 for all three weight configurations. The reported peak and loop objectives change little across the tested weight configurations.

In addition to the weighting study, we examine the sensitivity of inverse-control performance to perturbations of the Bouc–Wen parameters β and γ, which strongly influence loop width and reversal transitions. Using the saturation-mapped identification model as the reference, β and γ vary within 0.7–1.3 times their nominal values. Across the 49 resulting parameter combinations, $\mathrm{RMSE}_{\mathrm{cmd}}$ changes from 4.9 N to about 4.9–5.4 N, while $\mathrm{RMSE}_{\mathrm{des}}$ remains within 25.3–25.6 N. These results indicate that moderate perturbations affect mainly the local error near velocity reversal, but produce only small changes in the reported tracking errors over the tested parameter grid. Fig. 9 visualizes this trend.

6.4 Feedforward-control simulation validation

The four identified models are then embedded in the same inverse feedforward loop so that their control performance can be compared directly under the same conditions. Two metrics are used: $\mathrm{RMSE}_{\mathrm{des}}$ tracks F_{actual} against the initial F_{des} and

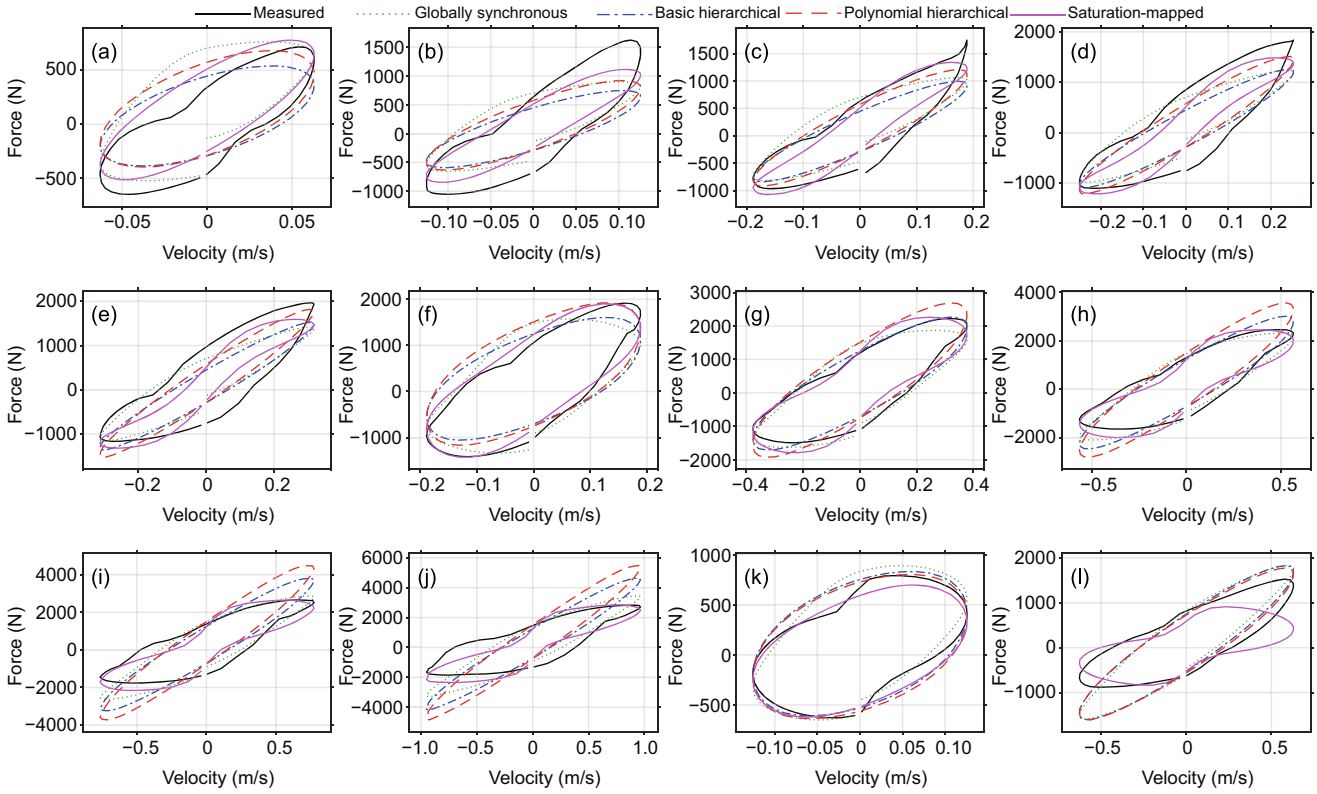


Fig. 6 Force–velocity profiles for the four models against the bench measurements: (a) $I = 1$ A, 1 Hz; (b) $I = 1$ A, 2 Hz; (c) $I = 1$ A, 3 Hz; (d) $I = 1$ A, 4 Hz; (e) $I = 1$ A, 5 Hz; (f) $I = 0.5$ A, 1 Hz; (g) $I = 0.5$ A, 2 Hz; (h) $I = 0.5$ A, 3 Hz; (i) $I = 0.5$ A, 4 Hz; (j) $I = 0.5$ A, 5 Hz; (k) $I = 0$ A, 1 Hz; (l) $I = 0$ A, 5 Hz

Table 3 Multi-objective optimization results of the saturation-mapped hierarchical model

Weight configuration	Weighted	Equal-weight	Peak	Loop objective
Balanced	0.082	0.079	0.074	0.0334
Peak-priority	0.077	0.075	0.074	0.0334
Loop-priority	0.076	0.073	0.074	0.0334

therefore includes the passivity clip, while $\mathrm{RMSE}_{\mathrm{cmd}}$ tracks F_{actual} against the feasible F_{cmd} and therefore measures the tracking accuracy relative to F_{cmd}.

Table 4 gives the simulation results. For the saturation-mapped model, $\mathrm{RMSE}_{\mathrm{cmd}}$ decreases to 4.9 N, whereas for the three other models, $\mathrm{RMSE}_{\mathrm{cmd}}$ is between 148.6 N and 216.5 N. The correlation coefficient reaches 1.000, and the RMS current is also the smallest at 0.887 A. This improvement therefore comes from a better inverse model rather than a more aggressive current demand.

Fig. 10 shows the corresponding time histories. For most of the stroke, F_{actual} remains close to F_{cmd}. The remaining mismatch is concentrated mainly near the reversal points, where hysteresis and unmodeled dynamics are the hardest to handle. The current trace shows repeated rapid transitions.

To probe the applicability range of the identified inverse model, additional frequency-sweep analysis has been conducted over 1–10 Hz at displacement amplitudes of 20, 40, and 60 mm. The plotted $\mathrm{RMSE}_{\mathrm{cmd}}$ varies across operating conditions and does not increase monotonically with frequency or displacement amplitude. Fig. 11 shows the trend of $\mathrm{RMSE}_{\mathrm{cmd}}$.

6.5 Hardware-in-the-loop bench validation

The controller is then tested on the HIL bench. The setup includes the host PC, current amplifier, CDC damper, and acquisition board, so practical effects such as driver delay, bandwidth limitation, and sensor noise are now present. The force sensor is still used only for offline evaluation.

Fig. 12 shows a representative HIL run. In Fig. 12a, F_{actual} follows the overall trend of F_{cmd}. The largest deviations appear near the force peaks and around direction reversal, where current lag and fast state transitions become more important.

The measured values are $\mathrm{RMSE}_{\mathrm{des}} = 111.9$ N and $\mathrm{RMSE}_{\mathrm{cmd}} = 136.3$ N. Although the HIL error is much larger than the simulation error, the controller still reproduces the main force trend, with a correlation coefficient of 0.981.

Fig. 12b compares the commanded current I_{cmd} with the applied current I_{app}. A visible phase lag and some amplitude attenuation appear during fast transients, and the current-lag RMSE reaches 0.253 A. Fig. 12c shows the force residuals, whose largest spikes occur near the velocity zero crossing. Fig. 12d presents the phase portrait, where the measurement data scatter away from the ideal tracking line because of

Table 4 Feedforward-control simulation performance of the four identification models

Model	$RMSE_{des}$ (N)	$RMSE_{cmd}$ (N)	Maximum absolute error (N)	Mean absolute error (N)	Correlation coefficient	RMS current (A)
Globally synchronous	151.7	148.6	537.5	118.5	0.990	1.007
Basic hierarchical	218.0	216.5	358.1	185.3	0.997	1.332
Polynomial hierarchical	212.4	210.2	376.0	179.1	0.994	1.270
Saturation-mapped hierarchical	**25.4**	**4.9**	**281.6**	**1.2**	**1.000**	**0.887**

The best results are in bold

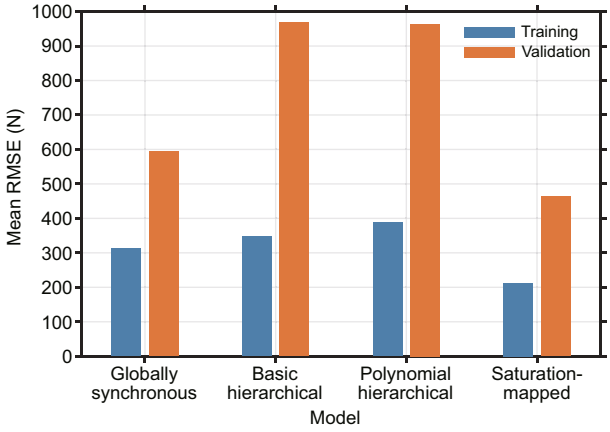


Fig. 7 Comparison of root-mean-squared errors for different modeling methods under multiple operating conditions

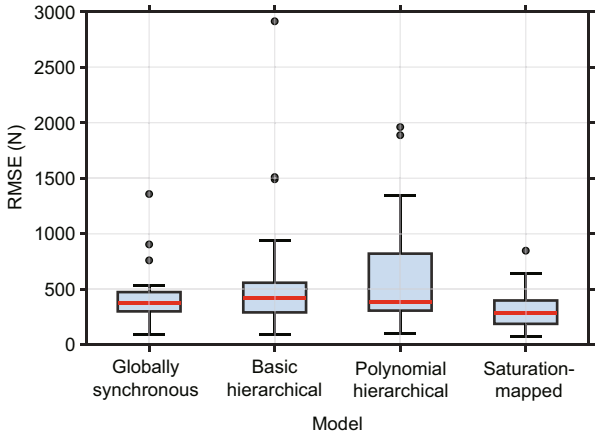


Fig. 8 Box-plot comparison of force-prediction RMSE for different identification methods under multiple operating conditions

bench-side dynamics.

The saturation ratio remains low, which indicates that one major error source is the amplifier dynamics rather than the current ceiling itself. In the simulation, $RMSE_{cmd}$ is only 4.9 N, whereas on the HIL bench it increases to 136.3 N. A natural next step is therefore to introduce driver-side dynamic compensation or current-loop refinement.

This interpretation is supported by an additional delay-oriented analysis of the drive chain. When the current path includes a first-order lag and pure delay, the same inverse controller shows a clear increase in the force-tracking error; for example, $RMSE_{cmd}$ rises from 4.9 N under the ideal path to 23.4 N for a representative case with a 5-ms lag and a 5-ms pure delay. Under this condition, the current-tracking error is about 0.225 A, close to the measured HIL value of 0.253 A.

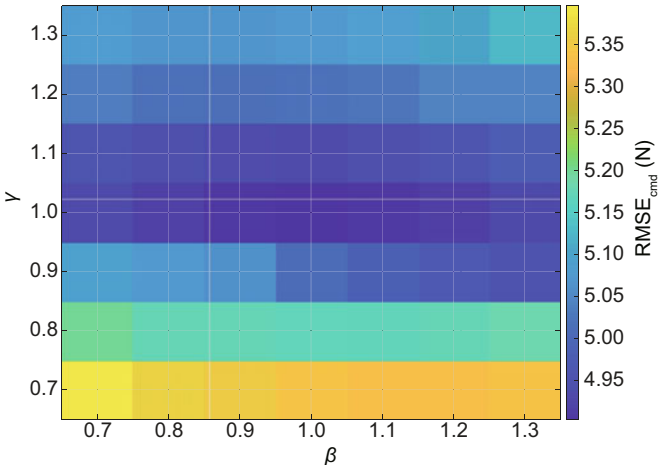


Fig. 9 Heat map of $RMSE_{cmd}$ under joint perturbations of Bouc–Wen parameters β and γ

These observations indicate that the HIL degradation is not caused solely by the static current–force mapping, but strongly affected by amplifier and valve dynamics. Fig. 13 shows the corresponding heat map. Future improvement may rely on a Smith predictor for nearly constant delay, inverse-dynamics prefiltering for first-order lag compensation, adaptive delay compensation for varying delays, and further refinement of the current loop using a joint model of the damper and drive dynamics.

7 Conclusions

This paper presents a systematic workflow for CDC damper force control, from bench characterization and dynamic modeling to real-time inverse force tracking. A four-component force model incorporating elastic restoring force, velocity-dependent viscous damping, Bouc–Wen hysteresis, and compression–rebound asymmetry is established, and its 20 parameters are calibrated via a three-stage hierarchical identification procedure that exploits the force-dominance region of each component. By decoupling the identification into elastic, damping, and hysteretic–asymmetric stages, the principal physical mechanisms are faithfully retained, while the ill-conditioning associated with direct global optimization is substantially alleviated. Ablation analysis further demonstrates that the staged strategy is effective only when the complete set of force mechanisms is preserved; removing the asymmetric term leads to a marked deterioration in validation accuracy.

Introducing exponential saturation functions to parameterize the current-dependent coefficients, in place of conventional polynomial maps, reduces the equal-weight identification error from 0.155 to 0.079. This bounded, monotonic

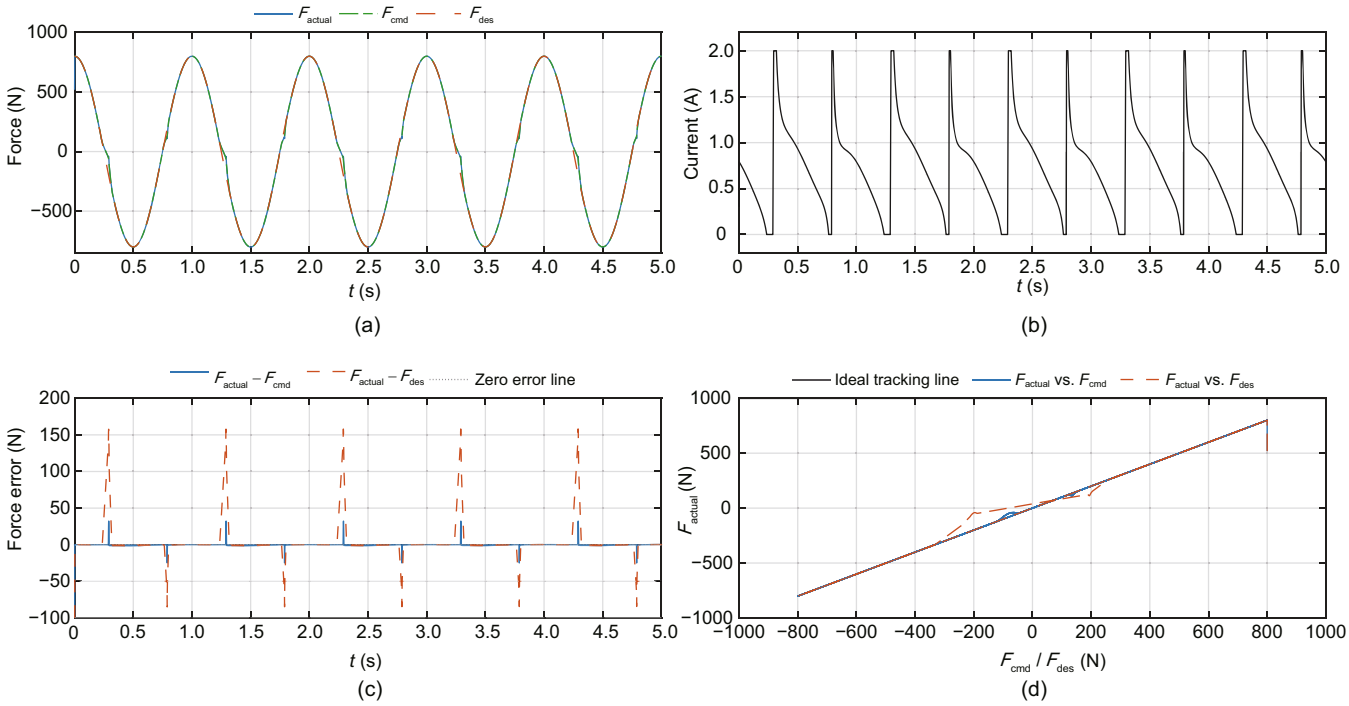


Fig. 10 Feedforward force-tracking behaviors in simulation using the saturation-mapped hierarchical model: (a) force time history; (b) control current; (c) tracking errors; (d) actual-versus-reference force comparison

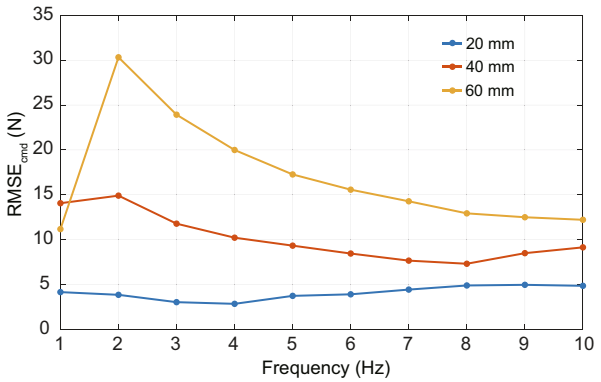


Fig. 11 Frequency-sweep trend of $RMSE_{cmd}$ from 1 to 10 Hz under different displacement amplitudes

parameterization simultaneously improves model generalization to the held-out operating-condition segments examined here, because every coefficient map remains bounded over the specified nonnegative current range.

Leveraging the identified model, a feedforward inverse controller based on the Newton iteration with online Bouc–Wen state reconstruction and passivity-based clipping achieves a simulation tracking $RMSE_{cmd}$ of 4.9 N, compared with 148.6 N for the globally synchronous model, without requiring any real-time force sensor. Hardware-in-the-loop experiments confirm that the proposed method achieves an $RMSE_{cmd}$ of 136.3 N in the reported bench test under practical amplifier bandwidth limitations and other bench-level non-idealities. The primary residual error is associated mainly with drive-chain dynamics, including amplifier transport delay, bandwidth limitation, and current response lag, rather than damper force saturation alone. Taken together, these results suggest that the combination of mechanism-based hierarchical identification and bounded inverse mapping may be explored for other nonlinear actuators subject to comparable passivity constraints.

Acknowledgments

This work was supported by the Wenzhou Key Scientific Research Project (No. ZGF2023056) and the National Natural Science Foundation of China (No. 52272376).

Author contributions

Shengdong YU designed the research framework, developed the methodology and software, and drafted the paper. Chengdi ZHANG conducted the hardware-in-the-loop experiments and organized the data. Chao CHEN contributed to validation and engineering resources. Hongming ZHOU contributed to formal analysis and investigation. Pengfei HAN supervised the project and acquired funding. Jinyu MA supervised the study, reviewed and edited the paper, and acquired funding.

Conflict of interest

All the authors declare that they have no conflict of interest.

Data availability

The data that support the findings of this study are available from the corresponding authors upon reasonable request.

Declaration on the use of generative AI tools

During the preparation of this work, the authors used DeepSeek for language polishing purposes only. After using this tool, the authors reviewed and edited the content as needed and take full responsibility for the content of the published article.

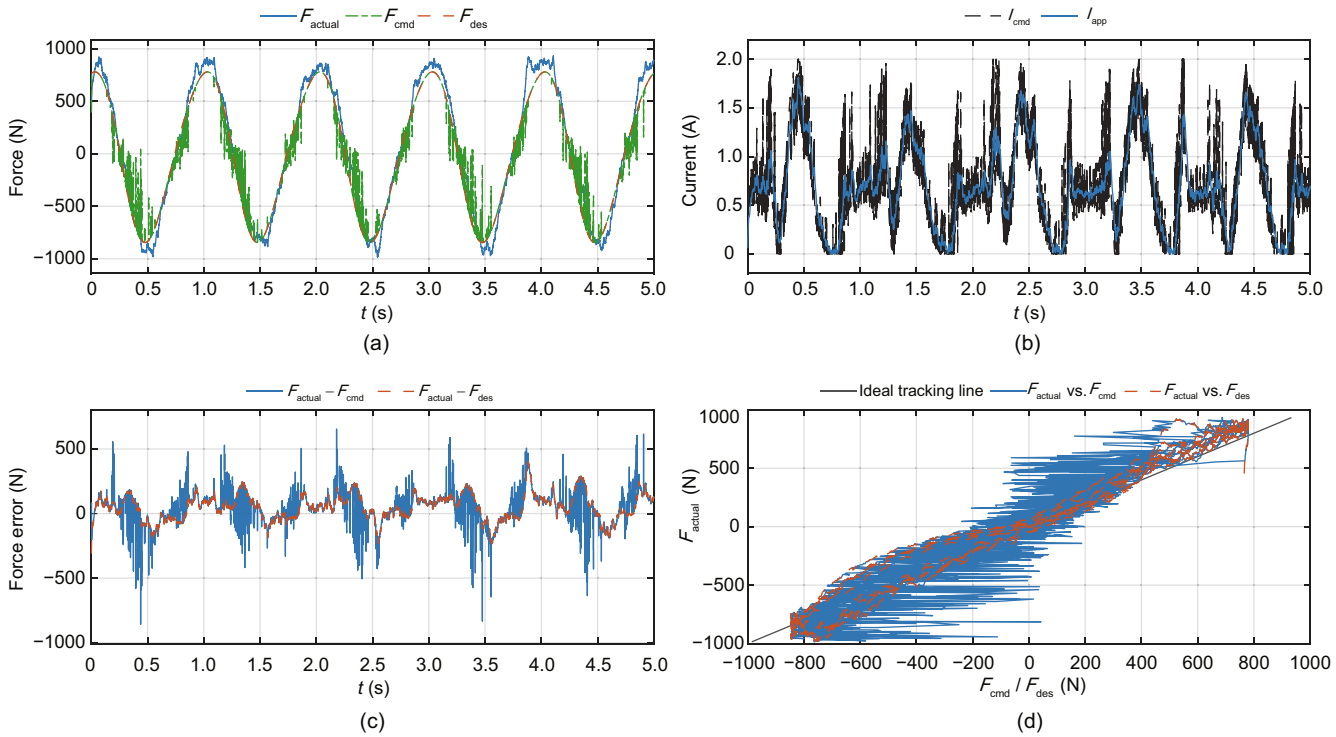


Fig. 12 Live feedforward force-tracking on the hardware-in-the-loop bench: (a) hardware force response; (b) comparison between I_{cmd} and I_{app}; (c) tracking errors; (d) actual-versus-reference comparison

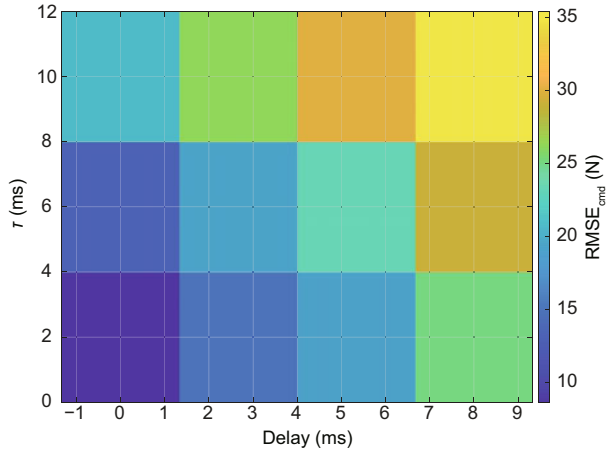


Fig. 13 Heat map of $RMSE_{cmd}$ under a first-order lag and pure delay in the drive chain

References

Cao Z, Zhao WJ, Hou XR, et al., 2020. Multi-objective robust control for vehicle active suspension systems via parameterized controller. *IEEE Access*, 8:7455-7465. https://doi.org/10.1109/ACCESS.2019.2963359

Fialho I, Balas GJ, 2002. Road adaptive active suspension design using linear parameter-varying gain-scheduling. *IEEE Trans Contr Syst Technol*, 10(1):43-54. https://doi.org/10.1109/87.974337

Gáspár P, Szabó Z, 2013. Design of a hierarchical controller for suspension systems. In: Sename O, Gáspár P, Bokor J (Eds.), Robust Control and Linear Parameter Varying Approaches: Application to Vehicle Dynamics. Springer, Berlin, Germany, p.311-328. https://doi.org/10.1007/978-3-642-36110-4_12

Gillespie TD, 1992. Fundamentals of Vehicle Dynamics. SAE, Warrendale, USA.

Karnopp D, 1995. Active and semi-active vibration isolation. *J Mech Des*, 117(B):177-185. https://doi.org/10.1115/1.2836452

Kimball JB, DeBoer B, Bubbar K, 2024. Adaptive control and reinforcement learning for vehicle suspension control: a review. *Annu Rev Contr*, 58:100974. https://doi.org/10.1016/j.arcontrol.2024.100974

Lee J, Oh K, 2025. Hybrid damping mode MR damper: development and experimental validation with semi-active control. *Machines*, 13(5):435. https://doi.org/10.3390/machines13050435

Li JH, Liao CR, Xie L, et al., 2023. Multi-stage hysteresis modelling of magnetorheological dampers and experimental verification. *Int J Mech Sci*, 254:108435. https://doi.org/10.1016/j.ijmecsci.2023.108435

Li PS, Nguyen AT, Du HP, et al., 2021. Polytopic LPV approaches for intelligent automotive systems: state of the art and future challenges. *Mech Syst Signal Process*, 161:107931. https://doi.org/10.1016/j.ymssp.2021.107931

Li T, Liao ZY, Cai Y, 2023. Reprint of: physical modeling for digital twin of continuous damping control damper. *J Manuf Process*, 100:55-63. https://doi.org/10.1016/j.jmapro.2023.06.002

Luan ZK, Cao XY, Zhao WZ, et al., 2025. Hierarchical dual-horizon preview control for CDC dampers and air springs in vehicle semi-active suspensions. *Sci China Technol Sci*, 68(10):2020801. https://doi.org/10.1007/s11431-025-3048-y

Ma JY, Xie MY, Chen PH, et al., 2023. Motion tracking of a piezo-driven cell puncture mechanism using enhanced sliding mode control with neural network. *Contr Eng Pract*, 134:105487. https://doi.org/10.1016/j.conengprac.2023.105487

Muthalif AGA, Razali MKM, Nordin NHD, et al., 2021. Parametric estimation from empirical data using particle swarm optimization method for different magnetorheological damper models. *IEEE Access*, 9:72602-72613. https://doi.org/10.1109/ACCESS.2021.3080432

Na J, Huang YB, Pei QQ, et al., 2020. Active suspension control of full-car systems without function approximation. *IEEE/ASME Trans Mechatron*, 25(2):779-791. https://doi.org/10.1109/TMECH.2019.2962602

Poussot-Vassal C, Sename O, Dugard L, et al., 2008. A new semi-active suspension control strategy through LPV technique. *Contr Eng Pract*, 16(12):1519-1534. https://doi.org/10.1016/j.conengprac.2008.05.002

Poussot-Vassal C, Spelta C, Sename O, et al., 2012. Survey and performance evaluation on some automotive semi-active suspension control methods: a comparative study on a single-corner model. *Annu Rev Contr*, 36(1):148-160. https://doi.org/10.1016/j.arcontrol.2012.03.011

Qin A, Zhang BJ, Ning DH, et al., 2024. A self-sensing approach for estimating suspension displacement and velocity in semi-active electromagnetic dampers. *Mech Syst Signal Process*, 208:111049. https://doi.org/10.1016/j.ymssp.2023.111049

Sename O, 2021. Review on LPV approaches for suspension systems. *Electronics*, 10(17):2120. https://doi.org/10.3390/electronics10172120

Shen YJ, Wang JS, Du F, et al., 2024. Dynamic performance analysis of semiactive vehicle ISD suspension based on the power-driven-damper strategy. *Shock Vib*, 2024(1):3495503. https://doi.org/10.1155/2024/3495503

Spencer BF, Dyke SJ, Sain MK, et al., 1997. Phenomenological model for magnetorheological dampers. *J Eng Mech*, 123(3):230-238. https://doi.org/10.1061/(ASCE)0733-9399(1997)123:3(230)

Wang F, Wen HS, Xie SS, 2025. Performance analysis and hybrid control strategy research of vehicle semi-active suspension for ride comfort and handling stability. *Machines*, 13(5):393. https://doi.org/10.3390/machines13050393

Wang ZM, Liu C, Zheng X, et al., 2024. Advancements in semi-active automotive suspension systems with magnetorheological dampers: a review. *Appl Sci*, 14(17):7866. https://doi.org/10.3390/app14177866

Wen YK, 1976. Method for random vibration of hysteretic systems. *J Eng Mech Div*, 102(2):249-263. https://doi.org/10.1061/JMCEA3.0002106

Wereley NM, Pang L, 1998. Nondimensional analysis of semi-active electrorheological and magnetorheological dampers using approximate parallel plate models. *Smart Mater Struct*, 7(5):732-743. https://doi.org/10.1088/0964-1726/7/5/015

Yang Y, Liu CN, Chen L, et al., 2024. Phase deviation of semi-active suspension control and its compensation with inertial suspension. *Acta Mech Sin*, 40(6):523367. https://doi.org/10.1007/s10409-023-23367-x

Yin ZJ, Wang R, Ma XG, et al., 2024. Fractional-order $PI^{\lambda}D^{\mu}$ control to enhance the driving smoothness of active vehicle suspension in electric vehicles. *World Electr Veh J*, 15(5):184. https://doi.org/10.3390/wevj15050184

Yu SD, Xie MY, Ma JY, et al., 2021. Precise robust motion tracking of a piezoactuated micropuncture mechanism with sliding mode control. *J Franklin Inst*, 358(8):4410-4434. https://doi.org/10.1016/j.jfranklin.2021.04.025

Yu SD, Xie MY, Wu HT, et al., 2022. Composite proportional-integral sliding mode control with feedforward control for cell puncture mechanism with piezoelectric actuation. *ISA Trans*, 124:427-435. https://doi.org/10.1016/j.isatra.2020.02.015

Yu SD, Wu HY, Kang SZ, et al., 2024. Model-free robust motion control for biological optical microscopy using time-delay estimation with an adaptive RBFNN compensator. *ISA Trans*, 149:365-372. https://doi.org/10.1016/j.isatra.2024.04.022

Yuan Q, Zhou HL, Chen SL, et al., 2023. Designing a switched Takagi–Sugeno fuzzy controller for CDC semi-active suspensions with current input constraint. *Mech Syst Signal Process*, 199:110450. https://doi.org/10.1016/j.ymssp.2023.110450

Yuan Q, Zhou HL, Chen SL, et al., 2025. Design and experimental validation of an asynchronous observer for CDC semi-active suspensions. *Contr Eng Pract*, 164:106471. https://doi.org/10.1016/j.conengprac.2025.106471